LETTER

doi:10.1038/nature13792

Piezoelectricity of single-atomic-layer MoS_2 for energy conversion and piezotronics

Wenzhuo Wu[1]*, Lei Wang[2]*, Yilei Li[3], Fan Zhang[4], Long Lin[1], Simiao Niu[1], Daniel Chenet[4], Xian Zhang[4], Yufeng Hao[4], Tony F. Heinz[3], James Hone[4] & Zhong Lin Wang[1,5]

The piezoelectric characteristics of nanowires, thin films and bulk crystals have been closely studied for potential applications in sensors, transducers, energy conversion and electronics[1–3]. With their high crystallinity and ability to withstand enormous strain[4–6], two-dimensional materials are of great interest as high-performance piezoelectric materials. Monolayer MoS_2 is predicted to be strongly piezoelectric, an effect that disappears in the bulk owing to the opposite orientations of adjacent atomic layers[7,8]. Here we report the first experimental study of the piezoelectric properties of two-dimensional MoS_2 and show that cyclic stretching and releasing of thin MoS_2 flakes with an odd number of atomic layers produces oscillating piezoelectric voltage and current outputs, whereas no output is observed for flakes with an even number of layers. A single monolayer flake strained by 0.53% generates a peak output of 15 mV and 20 pA, corresponding to a power density of 2 mW m^{-2} and a 5.08% mechanical-to-electrical energy conversion efficiency. In agreement with theoretical predictions, the output increases with decreasing thickness and reverses sign when the strain direction is rotated by 90°. Transport measurements show a strong piezotronic effect in single-layer MoS_2, but not in bilayer and bulk MoS_2. The coupling between piezoelectricity and semiconducting properties in two-dimensional nanomaterials may enable the development of applications in powering nanodevices, adaptive bioprobes and tunable/stretchable electronics/optoelectronics.

Crystal structure and symmetry dictate the physical properties of a material and its interaction with external stimuli. Materials with polarization domains, such as $Pb(Ti,Zr)O_3$, or with non-centrosymmetric structure, such as ZnO and GaN, are piezoelectric and have wide applications in sensors, transducers, power generation and electronics[1,3,9]. Layered materials, such as graphite, hexagonal boron nitride (h-BN) and many transition-metal dichalcogenides, are centrosymmetric in their bulk three-dimensional form but may exhibit different symmetry when thinned down to a single atomic layer[7,10,11]. In graphene, inversion symmetry is preserved because both atoms in the unit cell are identical, whereas monolayer h-BN and transition-metal dichalcogenides become non-centrosymmetric because of the absence of an inversion centre, which leads to novel properties such as valley-selective circular dichroism[12,13] and large second-order nonlinear susceptibility[14,15], corresponding to the optical second-harmonic generation (SHG) process[16]. Single-atomic-layer h-BN, MoS_2, $MoSe_2$ and WTe_2 have also been theoretically predicted to show piezoelectricity as a result of strain-induced lattice distortion and the associated ion charge polarization[7,8,11], suggesting possible applications of two-dimensional (2D) nanomaterials in nanoscale electromechanical devices that take advantage of their outstanding semiconducting and mechanical properties[4–6,17]. Here we report an experimental observation of piezoelectricity in single-atomic-layer 2D MoS_2 and its application in mechanical energy harvesting and piezotronic sensing. Cyclic stretching and releasing of odd-layer MoS_2 flakes produces oscillating electrical outputs, which converts mechanical energy into electricity. The strain-induced polarization charges in single-layer MoS_2 can also modulate charge carrier transport at the MoS_2–metal barrier and enable enhanced strain sensing. In addition, we have also observed large piezoresistivity in even-layer MoS_2 with a gauge factor of about 230 for the bilayer material, which indicates a possible strain-induced change in band structure[18]. Our study demonstrates the potential of 2D nanomaterials in powering nanodevices, adaptive bioprobes and tunable/stretchable electronics/optoelectronics.

In our experiments, MoS_2 flakes were mechanically exfoliated onto a polymer stack consisting of water-soluble polyvinyl alcohol and poly (methyl methacrylate) on a Si substrate, with the total polymer thickness tuned to be 275 nm for good optical contrast. Few-layer MoS_2 flakes were first identified under an optical microscope. The layer thickness was then measured by atomic force microscopy (Fig. 1a, inset) and confirmed by Raman spectroscopy (Extended Data Fig. 1a). SHG was subsequently used to determine the crystallographic orientation of the MoS_2 flakes (Methods and Extended Data Fig. 1b). Figure 1b shows a polar plot of the second-harmonic (SH) signal intensity from a single-layer MoS_2 flake as a function of the crystal's azimuthal angle. Here we measured the SH component perpendicular to the excitation polarization. The lattice orientation was determined by fitting the angle dependence of SH intensity with $I = I_0 \sin^2(3\theta)$, where θ denotes the angle between the direction of the 'armchair' edge and the polarization of the excitation laser, and I_0 is the maximum intensity of the SH response. Figure 1a schematically depicts the derived lattice orientation superimposed on the optical image of a single-layer MoS_2 flake; the x axis is taken to be along the 'armchair' direction, and the y axis along the 'zigzag' direction. After optical characterization, flakes were subsequently transferred to a polyethylene terephthalate (PET) flexible substrate using methods described previously[19]. Electrical contacts made of Cr/Pd/Au (1 nm/20 nm/50 nm) were deposited with the metal–MoS_2 interface parallel to the y axis. Figure 1c shows a typical flexible device with the single-layer MoS_2 flake outlined by black dashed line. When the substrate was bent mechanically, uniaxial strain is applied to the MoS_2 with a magnitude proportional to the inverse bending radius (Fig. 1d and Methods). The applied strain was limited to 0.8% to avoid sample slippage[20]. We studied the piezoelectric response by applying strain to a device coupled to an external load resistor (Fig. 1d). In this configuration, strain-induced polarization charges at the sample edges can drive the flow of electrons in external circuit[9]. When the substrate is released, electrons flow back in the opposite direction.

Figure 2a and Extended Data Fig. 3 show the piezoelectric current and voltage responses of a single-layer MoS_2. When strain is applied in the x direction ('armchair' direction), positive voltage and current output were observed with increasing strain, and negative output was observed with decreasing strain, directly demonstrating the conversion of mechanical energy into electricity[9] (see also Extended Data Fig. 4 and Methods). Both responses increased with the magnitude of the applied

[1]School of Materials Science and Engineering, Georgia Institute of Technology, Atlanta, Georgia 30332-0245, USA. [2]Department of Electrical Engineering, Columbia University, New York, New York 10027, USA. [3]Department of Physics, Columbia University, New York, New York 10027, USA. [4]Department of Mechanical Engineering, Columbia University, New York, New York 10027, USA. [5]Beijing Institute of Nanoenergy and Nanosystems, Chinese Academy of Sciences, 100083 Beijing, China.
*These authors contributed equally to this work.

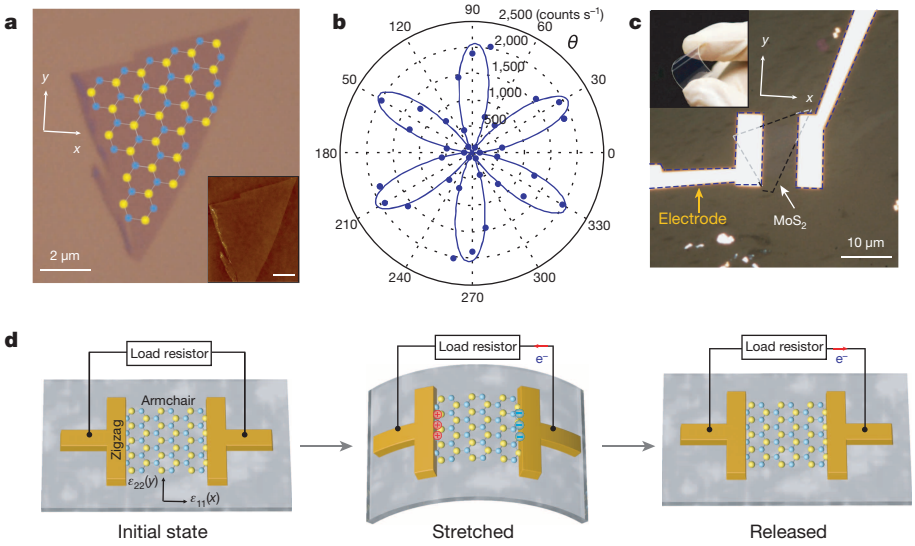

Figure 1 | Single-layer MoS_2 piezoelectric device and operation scheme. **a**, Optical image of the single-atomic layer MoS_2 flake with superimposed lattice orientation derived from SHG results. Blue and yellow spheres represent Mo and S atoms, respectively. Inset: atomic force microscopy image of the flake. Scale bar 2 μm. **b**, Polar plot of the SH intensity from single-layer MoS_2 as a function of the crystal's azimuthal angle θ. The symbols are experimental data and the solid lines are fits to the symmetry analysis described in the text. **c**, A typical flexible device with single-layer MoS_2 flake and electrodes at its zigzag edges. Inset: optical image of the flexible device. **d**, Operation scheme of the single-layer MoS_2 piezoelectric device. When the device is stretched, piezoelectric polarization charges of opposite polarity (plus and minus symbols) are induced at the zigzag edges of the MoS_2 flake. Periodic stretching and releasing of the substrate can generate piezoelectric outputs in external circuits with alternating polarity (as indicated by the red arrows).

strain: for single-layer MoS_2 with width of ~5 μm and a length of ~10 μm, the peak open-circuit voltage reached 18 mV and the peak short-circuit current reached 27 pA (Fig. 2b), with voltage and current responsivities of 55.1 ± 12.3 pA and 32.8 ± 4.5 mV, respectively, for each 1% change in strain. There were no significant electrical outputs from bare PET substrates without a single-layer MoS_2 flake (Extended Data Fig. 5b).

The dependence of piezoelectric charge polarization on the directions of principal strain in 2D materials was also investigated. The coupling between polarization (P_i) and strain (ε_{jk}) tensor can be quantified to first order by the third-rank piezoelectric tensor $e_{ijk} = (\partial P_i / \partial \varepsilon_{jk})$, where $i, j, k \in (1, 2, 3)$, with 1, 2 and 3 corresponding to the x, y and z axes, respectively. Symmetry analysis of the D_{3h} point group suggested that there was only one non-zero independent coefficient e_{11} for single-layer MoS_2. The in-plane polarization along the x axis, sensed by the metal electrodes as shown in Fig. 1d, can be expressed as $P_1 = e_{11}(\varepsilon_{11} - \varepsilon_{22})$, whereas P_2 along the y axis is related to the pure shear strain ε_{12} and can be ignored in these experiments. A distinctive consequence of this symmetry is that the output is expected to reverse sign when the strain is rotated from the x ('armchair') to the y ('zigzag') direction. This was verified experimentally, as shown in the bottom panel of Fig. 2a.

To quantify the power output of the piezoelectric circuit, it is necessary to study the voltage and current outputs as a function of load resistance, as shown in Fig. 2c (see Extended Data Fig. 6 for circuit details). The

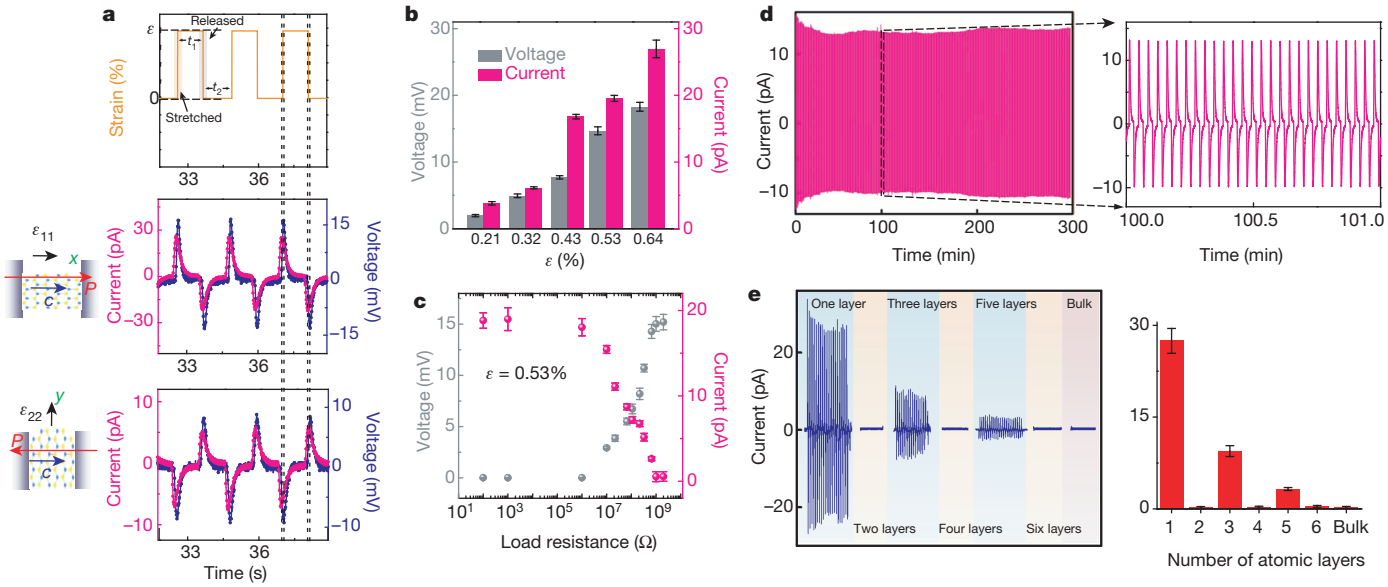

Figure 2 | Piezoelectric outputs from single-layer and multi-layer MoS_2 devices. **a**, Voltage response with 1 GΩ external load and short-circuit current response of a single-layer MoS_2 device under periodic strain in two different principal directions. Top: applied strain as a function of time. Middle: corresponding piezoelectric outputs from single-atomic-layer MoS_2 when strain is applied in the x direction (armchair direction). Bottom: corresponding piezoelectric outputs from the same device when strain is applied in the y direction (zigzag direction). The phase difference highlighted by black dashed lines is obtained by theoretical derivation and has been intentionally exaggerated for clarity, not experimental measurement. Red, blue and black arrows represent the directions of polarization, the polar axis of MoS_2 and principal strains, respectively. **b**, Dependence of piezoelectric outputs from a single-layer MoS_2 device on the magnitude of the applied strain. Mean values from 20 technical replicates are indicated. Error bars represent s.d. **c**, Dependence of voltage and current outputs from a single-layer MoS_2 device under 0.53% strain as a function of load resistance. Mean values from 20 technical replicates are indicated. Error bars represent s.d. **d**, Cyclic test showing the stability of single-layer MoS_2 device for prolonged period. **e**, Evolution of the piezoelectric outputs with increasing number of atomic layers (n) in MoS_2 flakes. For each device, mean values from 20 technical replicates are indicated. Error bars represent s.d.

output current was constant for a load resistance of up to ~1 MΩ and then decreased with increasing load, whereas the output voltage was ~0 V and began to increase at the same point. The maximum instantaneous power delivered to the load at 0.53% strain was achieved for a load resistance of ~220 MΩ and reached 55.3 fW (5.53×10^{-14} W), with a corresponding power density of 2 mW m^{-2} (Extended Data Fig. 6). The conversion efficiency of the single-layer MoS_2 nanogenerator, which is the ratio of the electric power delivered to the load to the total mechanical deformation energy stored in the single-layer MoS_2 after being strained, can therefore be estimated as ~5.08% (Methods). This energy conversion was stable over time, as shown for cyclic loading up to 0.43% strain at 0.5 Hz for 300 min (Fig. 2d and Extended Data Fig. 7). The observed slight decrease in output may have been caused by mechanical fatigue of the flexible substrate[9].

We next examined the evolution of the piezoelectric signal with an increasing number of atomic layers (n). As discussed above, because of the opposite orientation of alternating layers in the most common (2H) form of MoS_2, flakes with n = even are expected to be centrosymmetric and thus lose both their piezo response and SHG signal[8,16]. For the same reason, in samples with an odd number of layers, the piezo response and SHG should return. Figure 2e shows the measured piezoelectric output for MoS_2 flakes with n = 1, 2, 3, 4, 5 and 6, and for a bulk MoS_2 flake with a thickness of more than 100 nm. Consistent with the above picture, the SHG intensity was strong for n = 1, 3, 5 and disappeared for n = 2, 4, 6 and the bulk (Extended Data Fig. 8), consistent with previous reports[16]. To measure the piezoelectric response, the source and drain electrodes were made at the zigzag edge for the odd-layer flakes and at an arbitrary angle for the even-layer flakes, because of the absence of a SHG signal. Almost no detectable output can be seen for bulk flake and even-layer samples. For odd-layer samples the piezoelectric output is large and decreases roughly as the inverse of n. These results confirm that single-layer MoS_2 with broken inversion symmetry has a strong intrinsic piezoelectric response, whereas centrosymmetric bilayers and bulk crystals are non-piezoelectric[7,8].

We next characterized the changes in direct-current electrical transport properties of the devices with strain, in a two-terminal configuration with the polarity of the applied voltage defined with respect to the drain electrode. The metal–semiconductor–metal (MSM) device as fabricated consisted of two back-to-back Schottky barriers, and transport across the reverse-biased Pd–MoS_2 Schottky barrier limited the current flow[21]. In this configuration, changes in transport behaviour arose largely from two effects: the piezotronic effect[22], in which strain-induced charge asymmetrically modulated the Schottky barriers, and a piezoresistive effect, in which strain-induced bandgap change modulated the entire resistance of the device. For the single-layer device, the current–voltage curve shifted leftwards (towards negative drain bias) under tensile strain, and rightwards with compressive strain (Fig. 3a). The opposite trend was observed under negative drain bias. This asymmetric modulation was similar to the piezotronic effect reported for piezoelectric semiconductors with wurtzite and zincblende structures, in which the modulation of carrier transport arises as a result of piezoelectric polarization in the crystal (Methods). Here, piezoelectric polarization charges at the zigzag edges were able to affect the metal–MoS_2 contacts directly (Fig. 3c) by modifying the concentration or distribution of free carriers in MoS_2 as well as by modulating the electronic charges in interface states[22], such that the mechanical strain functioned as a controlling gate signal. Two points should be noted here. First, MoS_2 contacted Pd electrodes in two ways in our experiment: at its zigzag end edges, where the piezoelectric polarization charges were distributed, and at the top surface, which may not have had piezoelectric charges. Although the polarization charges were induced at the zigzag edge interface, they were still able to affect the electrical transport across the whole Schottky contact area formed between MoS_2 and metal. This was probably due to the fact that the majority electric field under bias was distributed at the end-edge contacts, in an analogous manner to previous studies on piezotronic effect in ZnO nanowires, in which the electric field was focused at the end surface although the contact also occurred at the side surfaces[23]. Second, the free charge carriers in monolayer MoS_2 were not taken into consideration for simplicity in the band diagrams (Fig. 3c). In reality, the finite carrier density in MoS_2 (which depended on factors such as intrinsic and environmental doping and varied from flake to flake) may have resulted in partial screening of the strain-induced polarization charges and hence could have affected its piezoelectric performance (Methods), but it is still possible to observe its piezoelectric power output and piezotronic transport characteristics. The results in Fig. 3a can be used to determine the crystallographic orientation of the flake uniquely as having the S-edge and Mo-edge at the drain and source electrodes, respectively. Controllable modulation of M–S contacts or p–n junctions in 2D nanomaterials by

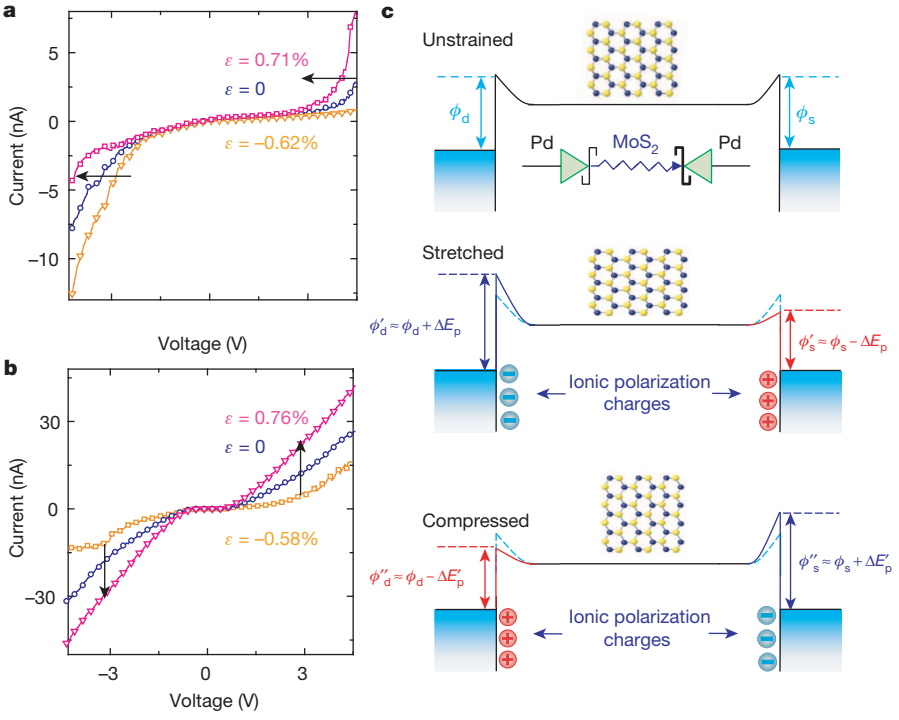

Figure 3 | Direct-current electrical characterizations of single-layer and bilayer MoS_2 devices under strains. **a**, The asymmetric modulation of carrier transport by strains under opposite drain bias in a single-layer device shows characteristics of a piezotronic effect. **b**, The symmetrical modulation of carrier transport by strains under opposite drain bias in a bilayer device shows characteristics of a piezoresistive effect. **c**, Band diagrams explaining the piezotronic behaviour observed in a single-layer device as a result of the changes in Schottky barrier heights by strain-induced polarization. ϕ_d and ϕ_s represent the Schottky barrier heights formed at drain and source contacts, respectively. E_p indicates the change in Schottky barrier height by piezoelectric polarization charges.

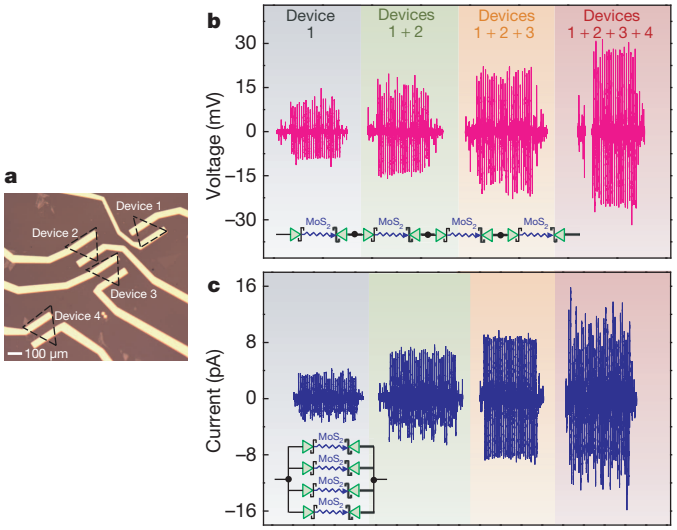

Figure 4 | Array integration of CVD single-layer MoS_2 flakes. **a**, Optical image of an array consisting of four CVD single-layer MoS_2 flakes. **b**, Constructive voltage outputs by serial connection of the individual flakes in the circuit. **c**, Constructive current outputs by parallel connection of the individual flakes in the circuit.

strain-induced polarization may offer a novel approach unavailable to conventional technologies using electrical control signals, without modifying the interface structure or chemistry, for implementing tunable electronics/optoelectronics, enhanced photovoltaics, hybrid spintronics and catalysis[24,25].

In bilayer and bulk MoS_2 devices, the response is purely piezoresistive: the current increases symmetrically with applied strain, and the gap region in the I–V curve shrinks, consistent with a lowering of both source and drain Schottky barriers as a result of a decrease in the bandgap[18] and/or a change in carrier density (see Fig. 3b for a bilayer device and Extended Data Fig. 9 for a bulk device). The gauge factors ($[\Delta I(\varepsilon)/I(0)]/\Delta\varepsilon$) of the bilayer (~230) and bulk MoS_2 devices (~200) measured in our experiments were comparable to that reported for a state-of-the-art silicon strain sensor (~200), and exceeded the values of conventional metal strain gauges (~1–5) and a graphene strain sensor (~2) (ref. 26). This is a preliminary demonstration of large piezoresistivity in 2D MoS_2, and motivates further study for using it in highly sensitive strain sensing.

Finally, we demonstrate the array integration of single-layer MoS_2 flakes to boost the piezoelectric output for energy conversion (Fig. 4). High-quality single-layer MoS_2 crystals were grown by seed-free chemical vapour deposition (CVD) on a Si/SiO_2 substrate, using a method reported previously[27]. Single-domain triangles were then transferred from the growth substrate to flexible PET[19]. Previous studies noted that molybdenum zigzag and sulphur zigzag are the two dominant morphologies of CVD MoS_2 triangles[28], and molybdenum zigzag triangles consistently have sharper and straighter edges than sulphur zigzag triangles[27]. This morphological difference allowed us to easily identify the crystal orientation of CVD MoS_2 in optical images and pattern the electrodes accordingly (Fig. 4a). For this demonstration, four CVD MoS_2 flakes were chosen. By constructively connecting the four flakes either in series or in parallel, consistent enhancements in output voltages or currents were observed (Fig. 4b, c). Moreover, by destructively connecting devices 1 and 2 either in series or in parallel, the combined outputs were the difference of the two individual outputs (Extended Data Fig. 10). This may open up possibilities of achieving practical technology at an even larger scale with 2D piezoelectric nanomaterials for powering nanodevices, tactile imaging and wearable electronics[9,29]. Nevertheless, efforts are required to achieve a better understanding of the synthesis of CVD MoS_2 with more controllable properties and optimize large-scale fabrication for improving device-to-device uniformity and achieving practical applications based on an array of single-atomic-layer MoS_2 devices.

The piezoelectricity and large mechanical stretchablity and flexibility of single-atomic-layer MoS_2 demonstrate its potential applications in electromechanical sensing, wearable technology, pervasive computing and implanted devices. The integration of a MoS_2-based power source with graphene and other functional units or devices based on 2D materials for energy storage, sensing, logic computation and communication on the same substrate may permit the construction of an atomic-thin self-powered nanosystem that can operate self-sustainably without external bias by harvesting energy from the ambient environment[30], especially in circumstances in which other energy sources, such as solar or thermal energy, are not readily available.

Online Content Methods, along with any additional Extended Data display items and Source Data, are available in the online version of the paper; references unique to these sections appear only in the online paper.

Received 23 May; accepted 8 August 2014.
Published online 15 October 2014.

1. Kingon, A. I. & Srinivasan, S. Lead zirconate titanate thin films directly on copper electrodes for ferroelectric, dielectric and piezoelectric applications. *Nature Mater.* **4,** 233–237 (2005).
2. Ferren, R. A. Advances in polymeric piezoelectric transducers. *Nature* **350,** 26–27 (1991).
3. Wang, Z. L. & Song, J. H. Piezoelectric nanogenerators based on zinc oxide nanowire arrays. *Science* **312,** 242–246 (2006).
4. Lee, C., Wei, X. D., Kysar, J. W. & Hone, J. Measurement of the elastic properties and intrinsic strength of monolayer graphene. *Science* **321,** 385–388 (2008).
5. Lee, G. H. *et al.* High-strength chemical-vapor deposited graphene and grain boundaries. *Science* **340,** 1073–1076 (2013).
6. Bertolazzi, S., Brivio, J. & Kis, A. Stretching and breaking of ultrathin MoS_2. *ACS Nano* **5,** 9703–9709 (2011).
7. Duerloo, K. A. N., Ong, M. T. & Reed, E. J. Intrinsic piezoelectricity in two-dimensional materials. *J. Phys. Chem. Lett.* **3,** 2871–2876 (2012).
8. Michel, K. H. & Verberck, B. Phonon dispersions and piezoelectricity in bulk and multilayers of hexagonal boron nitride. *Phys. Rev. B* **83,** 115328 (2011).
9. Yang, R. S., Qin, Y., Dai, L. M. & Wang, Z. L. Power generation with laterally packaged piezoelectric fine wires. *Nature Nanotechnol.* **4,** 34–39 (2009).
10. Ong, M. T. & Reed, E. J. Engineered piezoelectricity in graphene. *ACS Nano* **6,** 1387–1394 (2012).
11. Michel, K. H. & Verberck, B. Theory of elastic and piezoelectric effects in two-dimensional hexagonal boron nitride. *Phys. Rev. B* **80,** 224301 (2009).
12. Mak, K. F., He, K. L., Shan, J. & Heinz, T. F. Control of valley polarization in monolayer MoS_2 by optical helicity. *Nature Nanotechnol.* **7,** 494–498 (2012).
13. Zeng, H. L., Dai, J. F., Yao, W., Xiao, D. & Cui, X. D. Valley polarization in MoS_2 monolayers by optical pumping. *Nature Nanotechnol.* **7,** 490–493 (2012).
14. Kumar, N. *et al.* Second harmonic microscopy of monolayer MoS_2. *Phys. Rev. B* **87,** 161403 (2013).
15. Malard, L. M., Alencar, T. V., Barboza, A. P. M., Mak, K. F. & de Paula, A. M. Observation of intense second harmonic generation from MoS_2 atomic crystals. *Phys. Rev. B* **87,** 201401 (2013).
16. Li, Y. L. *et al.* Probing symmetry properties of few-layer MoS_2 and h-BN by optical second-harmonic generation. *Nano Lett.* **13,** 3329–3333 (2013).
17. Wang, Q. H., Kalantar-Zadeh, K., Kis, A., Coleman, J. N. & Strano, M. S. Electronics and optoelectronics of two-dimensional transition metal dichalcogenides. *Nature Nanotechnol.* **7,** 699–712 (2012).
18. Conley, H. J. *et al.* Bandgap engineering of strained monolayer and bilayer MoS_2. *Nano Lett.* **13,** 3626–3630 (2013).
19. Dean, C. R. *et al.* Boron nitride substrates for high-quality graphene electronics. *Nature Nanotechnol.* **5,** 722–726 (2010).
20. He, K., Poole, C., Mak, K. F. & Shan, J. Experimental demonstration of continuous electronic structure tuning via strain in atomically thin MoS_2. *Nano Lett.* **13,** 2931–2936 (2013).
21. Neal, A. T., Liu, H., Gu, J. J. & Ye, P. D. in *Conference Digest, Device Research Conference (DRC), 18–20 June 2012 70th Annual* 65–66, http://dx.doi.org/10.1109/DRC.2012.6256928 (IEEE, 2012).
22. Wang, Z. L. Piezopotential gated nanowire devices: piezotronics and piezo-phototronics. *Nano Today* **5,** 540–552 (2010).
23. Hu, Y. F. *et al.* Temperature Dependence of the Piezotronic Effect in ZnO Nanowires. *Nano Lett.* **13,** 5026–5032 (2013).
24. Chen, J. R. *et al.* Control of Schottky barriers in single layer MoS_2 transistors with ferromagnetic contacts. *Nano Lett.* **13,** 3106–3110 (2013).
25. Yang, H. *et al.* Graphene barristor, a triode device with a gate-controlled Schottky barrier. *Science* **336,** 1140–1143 (2012).
26. Huang, M. Y., Pascal, T. A., Kim, H., Goddard, W. A. & Greer, J. R. Electronic-mechanical coupling in graphene from in situ nanoindentation experiments and multiscale atomistic simulations. *Nano Lett.* **11,** 1241–1246 (2011).
27. van der Zande, A. M. *et al.* Grains and grain boundaries in highly crystalline monolayer molybdenum disulphide. *Nature Mater.* **12,** 554–561 (2013).

28. Lauritsen, J. V. *et al.* Size-dependent structure of MoS_2 nanocrystals. *Nature Nanotechnol.* **2,** 53–58 (2007).
29. Wu, W. Z., Wen, X. N. & Wang, Z. L. Taxel-addressable matrix of vertical-nanowire piezotronic transistors for active and adaptive tactile imaging. *Science* **340,** 952–957 (2013).
30. Wang, Z. L. & Wu, W. Z. Nanotechnology-enabled energy harvesting for self-powered micro-/nanosystems. *Angew. Chem. Int. Ed.* **51,** 11700–11721 (2012).

Acknowledgements We thank C. Dean, P. Kim and K. Shepard for discussions, and K. Alexander and E. Reed for theoretical consultation. This research was supported by the US Department of Energy, Office of Basic Energy Sciences (DE-FG02-07ER46394) and US National Science Foundation (DMR-1122594). Z.L.W. acknowledges the 'Thousands Talents' programme for pioneer researcher and his innovation team, National Natural Science Foundation of China (51432005), and China and Beijing City Committee of Science and Technology (Z131100006013004 and Z131100006013005).

Author Contributions W.Z.W., L.W., Z.L.W. and J.H. conceived the idea. W.Z.W., L.W., Y.L.L., T.F.H., J.H. and Z.L.W. designed the experiments. L.W., D.C., F.Z. and Y.F.H. synthesized the material. L.W., D.C. and W.Z.W. fabricated the devices. Y.L.L. performed the SHG characterization. W.Z.W., L.W., L.L., Y.L.L. and S.M.N. conducted the experiments. W.Z.W., L.W., J.H. and Z.L.W. analysed the data and wrote the manuscript.

Author Information Reprints and permissions information is available at www.nature.com/reprints. The authors declare no competing financial interests. Readers are welcome to comment on the online version of the paper. Correspondence and requests for materials should be addressed to Z.L.W (zhong.wang@mse.gatech.edu) or J.H. (jh2228@columbia.edu).

METHODS

Determination of crystallographic orientation in MoS_2 flakes by optical SHG. The SHG measurements were performed in reflection geometry (Extended Data Fig. 1b). The incident excitation beam was normal to the sample. The pump radiation was supplied by a mode-locked Ti:sapphire oscillator operating at a repetition rate of 80 MHz. The pulses were of 90 fs duration and centred on a wavelength of 810 nm. Using a ×100 objective, we focused the pump beam on the sample with a spot size of about 1 μm. We limited the average laser power to 1 mW. The retro-reflected SH signal was collected by the same objective, separated by a beam splitter and filtered by a short-pass optical filter (cutoff at 785 nm) to block the reflected fundamental radiation. An analyser was used to select the polarization component of the SH radiation perpendicular to the polarization of the pump beam. After dispersal in a spectrometer, the SH signal was detected by a liquid-nitrogen-cooled charge-coupled device camera. The SH character of the detected radiation was verified by its wavelength and quadratic power dependence on the pump intensity. In our setup we could freely rotate the samples to obtain the orientation dependence of the SH response. However, it should be noted that the lattice orientation cannot be uniquely determined by SHG because the SH signal remains the same if the lattice plane is rotated by 180° with respect to its normal direction. In other words, only the direction of the Mo–S bond axis can be obtained from the SHG signal, and no conclusion can be drawn about which side is Mo-edge or S-edge.

Electrical output measurements. A programmable electrometer (part number 6514, Keithley) with 200 TΩ input impedance was used for measuring voltage signals from the device. A low-noise current preamplifier (part number SR570; Stanford Research Systems, Inc.) was used for current measurements, with its direct-current input impedance at 1 MΩ for the sensitivity level used (10^{-11} and 10^{-12} A V^{-1}). A 10-Hz low-pass filter was used for both voltage and current measurements. A computer-controlled measurement software written in Labview was used to collect and record the data. All measurements were made inside a home-built electrical cage. A linear motor (LinMot PS01-23 × 80) was used for applying programmed driving strain inputs.

Estimation of strain induced in MoS_2 device. Because the dimensions of MoS_2 flakes (5 μm × 5 μm × (0.6–100 nm)) are significantly smaller than those of the PET substrates (2.5 cm × 2 cm × 500 μm), the mechanical behaviour of the substrate and entire device is not affected by the MoS_2 flake. Consequently, the Saint-Venant theory for small bending deformation can be adopted for estimating the induced strain in MoS_2 devices[31]. The PET substrate can be approximated as a beam structure of thickness a, width w and length l. The origin for calculation is defined as the centre of the fixed edge. The x and z axis are along the width (w) and length (l) directions of the substrate, respectively (Extended Data Fig. 2a). Because the MoS_2 flake lies above the neutral strain axis of the entire device, the deflection of the substrate under an external force f_y, exerted by the linear motor, results in a pure elongation or contraction in the MoS_2 flake if no slippage is considered. It follows that the uniaxial in-plane strain induced in MoS_2 can be estimated by the ε_{zz} component of strain in the PET substrate. Applying the Saint-Venant theory for small deflections of the beam, $\sigma_z z = -(f_y/I_{xx})y(l-z)$, $\sigma_{xx} = \sigma_{yy} = 0$, in which I_{xx} is the moment of inertia for the beam. Consequently, $\varepsilon_{zz} = \sigma_{zz}/E$, where E is the Young's modulus of substrate. Experimentally, it is more convenient to measure the lateral deflection D_{max} of the free end of substrate rather than the external point force f_y. Since $D_{max} = f_y l^3/3EI_{xx}$ by classical beam mechanics, then

$$\varepsilon_{zz} = -\frac{3y}{l}\frac{D_{max}}{l}\left(1-\frac{z}{l}\right)$$

Because the MoS_2 flake is lying at $y = \pm a/2$ and $z = z_0$, where z_0 is the distance between the fixed edge and the MoS_2 flake, which can be measured in the experiment, the strain induced in MoS_2 flake can be estimated by

$$\varepsilon = \varepsilon_{zz} = \mp 3\frac{a}{2l}\frac{D_{max}}{l}\left(1-\frac{z_0}{l}\right) \quad (1)$$

The negative sign is for compressive strain and positive sign is for tensile strain. All variables in the above equation can be readily measured experimentally. In the experiment, the linear motor used for inducing strain is first accelerated and then decelerated with a constant acceleration a. The maximum lateral deflection D_{max} of the free end of the substrate, the acceleration a and the hold time (t_1 and t_2) are known parameters and can be controlled by the linear motor (see Extended Data Fig. 2b, c). Therefore the driving signal (moving distance d) in one cycle can be mathematically described by the following equations:

$$d = at^2/2,\ (t < \sqrt{D_{max}/a})$$

$$d = D_{max} - \frac{1}{2}a\left(2\sqrt{D_{max}/a} - t\right)^2,\ (\sqrt{D_{max}/a} \le t < 2\sqrt{D_{max}/a})$$

$$d = D_{max},(2\sqrt{D_{max}/a} \le t < 2\sqrt{D_{max}/a} + t_1)$$

$$d = D_{max} - \frac{1}{2}a\left(t - 2\sqrt{D_{max}/a} - t_1\right)^2,(2\sqrt{D_{max}/a} + t_1 \le t < 3\sqrt{D_{max}/a} + t_1)$$

$$d = \frac{1}{2}a\left(t - 4\sqrt{D_{max}/a} - t_1\right)^2,(3\sqrt{D_{max}/a} + t_1 \le t < 4\sqrt{D_{max}/a} + t_1)$$

$$d = 0,(4\sqrt{D_{max}/a} + t_1 \le t < 4\sqrt{D_{max}/a} + t_1 + t_2)$$

A representative plot is shown in Fig. 2a and Extended Data Fig. 2b. As a result of the large difference between scales of a (5–10 m s^{-2}) and D_{max} (<10 mm), the stretch and release edges of the strain curve are very sharp. Snapshots from the typical configurations of the linear motor are also included in Extended Data Fig. 2c.

Power generation by piezoelectric polarization charges in single-layer MoS_2. When single-layer MoS_2 is subjected to tensile strain, effective piezoelectric charges are induced at the armchair edges as a result of the polarization of atoms in the strained crystal (Extended Data Fig. 4b). The negative polarization charges deplete the barrier interface and drive the electron flow from the left electrode to the right electrode through an external load (Extended Data Fig. 4b), giving rise to the current peak labelled 'b' in Extended Data Fig. 4. The resistance of the Schottky barrier is significantly high for voltages below a threshold value and thus blocks the flow of electrons through the wire (Extended Data Fig. 4b). The electrons accumulate at the interfacial region between the right electrode and the MoS_2; the effect of piezoelectric polarization charges is balanced by the accumulated electrons and the Fermi levels in the entire system reach a new equilibrium (Extended Data Fig. 4c). When the tensile strain in the MoS_2 is released, the piezoelectric polarization charges vanish immediately and the electrons previously accumulated at the right electrode flow back to the left electrode through the external load to return the system to the original state, resulting in the downward current peak labelled 'd' in Extended Data Fig. 4. The above process therefore performs one cycle of energy harvesting and conversion from the mechanical to the electrical domain by single-layer MoS_2.

The piezoelectric voltage constant g is the electric field generated by a piezoelectric material per unit of mechanical stress applied or, alternatively, is the mechanical strain experienced by a piezoelectric material per unit of electric displacement applied. The first subscript to g indicates the direction of the electric field generated in the material, or the direction of the applied electric displacement. The second subscript is the direction of the applied stress or the induced strain, respectively. The strength of the induced electric field produced by a piezoelectric material in response to an applied physical stress is the product of the value for the applied stress and the value for g. For simplicity we can assume that the piezoelectric material is an insulator with no internal screening of the strain-induced polarization charges and that the Schottky barrier between the piezoelectric material and the metal electrode can fully block the electron injection from metal electrode back to the piezoelectric material. Therefore, if we apply a strain ε to the piezoelectric material, the internal piezoelectric field generated inside the piezoelectric material is given by $E = g\varepsilon Y$, where g is piezoelectric voltage constant and Y is the Young's modulus of the piezoelectric material. Thus, the internal piezoelectric potential across the piezoelectric material can be given by $V_{piezo} = Eh = g\varepsilon Yh$, where h is the length of the material. Thus, at open-circuit condition, the voltage between the two electrodes is this internal piezoelectric potential. Therefore $V_{OC} = V_{piezo} = Eh = g\varepsilon Yh$.

We assume that the piezoelectric material is insulating and that the Schottky barrier between the piezoelectric material and the metal electrode can fully block the electron injection from the metal electrode back to the piezoelectric material. Thus, when the two electrodes are connected by an external load, the electrons will be driven to flow from one electrode to the other. These transferred electrons will generate another electric field, which will screen the original piezoelectric field generated by the strain. If the transferred charge amount from one electrode to the other electrode is Q, the voltage generated by those charges can be shown to be Q/C_0, where C_0 is the capacitance between the two electrodes, which can be roughly estimated as a constant. Under short-circuit conditions, the total potential drop between the two electrodes is 0. Thus, we have $V_{piezo} = Q_{SC}/C_0$. The short-circuit transferred charge can be given by $Q_{SC} = C_0 V_{piezo} = C_0 g\varepsilon Yh$. Therefore the short-circuit current can be shown to be

$$I_{SC} = \frac{dQ_{SC}}{dt} = C_0 gYh\frac{d\varepsilon}{dt}$$

In our experiment, the equivalent resistance of the piezoelectric nanogenerator (mainly contributed by the reverse-biased Schottky barrier) is ~80 GΩ when the bias is close to zero (at ~20 mV), which can be obtained from Fig. 3a. Because the largest load resistance used in power output measurement (Fig. 2) is 2 GΩ, we can consider that the internal resistance of the piezoelectric nanogenerator to be infinite, and the Schottky barrier between the piezoelectric material and the metal electrode

can fully block electron injection from the metal electrode back to the piezoelectric material. Therefore the piezoelectric nanogenerator can be assumed to be purely capacitive. When the nanogenerator is connected with a load resistor, the equivalent circuit for the whole system is shown in Extended Data Fig. 4.

We first analyse a simple case when the mechanical motion is a pure harmonic vibration: $\varepsilon = A\sin(\omega t)$. Thus, from the above analysis, $V_{\text{piezo}} = g\varepsilon Yh = gAYh\sin(\omega t)$. And C_0 can be assumed constant, as discussed above. The whole system is a linear time-invariant system and a phase method can be used to solve the system. The following equations for the output voltage and current with a load resistance of R can be obtained:

$$I_R = \frac{1}{(1/j\omega C_0)+R} gAYh = gAYh\frac{\omega C_0}{1+\omega^2R^2{C_0}^2}(\omega RC_0 + j)$$

$$V_R = \frac{R}{(1/j\omega C_0)+R} gAYh = gAYh\frac{\omega RC_0}{1+\omega^2R^2{C_0}^2}(\omega RC_0 + j)$$

Therefore

$$I_R(t) = gAYh\frac{\omega C_0}{1+\omega^2R^2{C_0}^2}(\omega RC_0\sin(\omega t) + \cos(\omega t))$$

$$V_R(t) = gAYh\frac{\omega RC_0}{1+\omega^2R^2{C_0}^2}(\omega RC_0\sin(\omega t) + \cos(\omega t))$$

The short-circuit current is then

$$I_{\text{SC}} = gAYh\omega C_0\cos(\omega t)$$

Therefore the phase shift θ between the short-circuit current and non-open-circuit voltage (finite external load) can be obtained as $\theta = 90 - \arctan(1/\omega RC_0)$. Therefore, when $R = 0$ the phase shift between the output signal and the short-circuit current is 0, and when $R = \infty$ the phase shift between the output signal and the short circuit current is 90°. For other cases, the phase difference is between 0° and 90°.

When the applied strain is not pure harmonic, because the applied strain is still a periodic signal it can be presented as a Fourier series:

$$\varepsilon = \sum_{k=1}^{\infty} A_1\sin(k\omega t) + B_1\cos(k\omega t)$$

Because the system is a still linear time-invariant system, the output is a summation of the output of each harmonic signal. From the similar analysis, we can still obtain a similar conclusion:

$$V_{\text{piezo}} = g\varepsilon Yh = gYh\left(\sum_{k=1}^{\infty} A_1\sin(k\omega t) + B_1\cos(k\omega t)\right)$$

$$I_R(t) = gYh\sum_{k=1}^{\infty} A_1\left(\frac{k\omega C_0}{1+k^2\omega^2R^2C_0^2}(k\omega RC_0\sin(k\omega t) + \cos(k\omega t))\right) + B_1\left(\frac{k\omega C_0}{1+k^2\omega^2R^2C_0^2}(k\omega RC_0\cos(k\omega t) - \sin(k\omega t))\right)$$

$$V_R(t) = gYh\sum_{k=1}^{\infty} A_1\left(\frac{kR\omega C_0}{1+k^2\omega^2R^2C_0^2}(k\omega RC_0\sin(k\omega t) + \cos(k\omega t))\right) + B_1\left(\frac{kR\omega C_0}{1+k^2\omega^2R^2C_0^2}(k\omega RC_0\cos(k\omega t) - \sin(k\omega t))\right)$$

When $R = 0$,

$$I_{\text{SC}}(t) = gYh\omega C_0\sum_{k=1}^{\infty}(A_1k\cos(k\omega t) - B_1k\sin(k\omega t))$$

When $R = \infty$,

$$V_{\text{OC}}(t) = gYh\left(\sum_{k=1}^{\infty} A_1\sin(k\omega t) + B_1\cos(k\omega t)\right)$$

When $R \ll |1/\omega C_0|$, it can be easily seen that $I_R(t)$ converges to I_{SC}, and that when $R \gg |1/\omega C_0|$, $V_R(t)$ converges to V_{OC}.

Consequently, on the basis of the above discussions for the two cases, there is a phase difference between the signals of the short-circuit current and non-open-circuit voltage. The difference depends on the internal impedance of the piezoelectric nanogenerator and the external load resistance. Similarly, there is also a difference between the signals of the open-circuit voltage and the short-circuit current: the piezoelectric open-circuit voltage signal peaks when the strain reaches a maximum value, and the piezoelectric short-circuit current signal peaks when the strain rate reaches a maximum. It should be noted that the phase difference highlighted by black dashed lines was obtained by theoretical derivation for an ideal case; it was not measured experimentally because of the limitation in the experimental setup.

Moreover, the following relationship between acceleration a, maximum speed $v_{\max}$ and the total moving distance d (with maximum deflection $D_{\max}$) can be obtained: $v_{\max}^2 = 2aD_{\max}/2 = aD_{\max}$, because $\varepsilon \propto d$, and

$$I_{\text{SC}} = \frac{\mathrm{d}Q_{\text{SC}}}{\mathrm{d}t} = C_0gYh\frac{\mathrm{d}\varepsilon}{\mathrm{d}t}$$

$$I_{\text{SC,max}} = C_0gYhkv_{\max} = C_0gYhk\sqrt{aD_{\max}}$$

Therefore, when we increase either the acceleration or the total moving distance $D_{\max}$, the magnitude of the short-circuit current will increase. The hysteresis observed for the short-circuit current and the open-circuit voltage under strain can also be understood from the above discussion (Extended Data Fig. 5a).

Estimation of power generation efficiency by MoS_2. The total mechanical deformation energy stored in the monolayer MoS_2 after being strained is calculated by $W_M = LWE\varepsilon^2/2$, where E is the 2D elastic modulus of MoS_2 (130 N m^{-1})[32], L is the distance between the two electrodes, and W is the width of the MoS_2 flake. The total electric energy generated through the piezoelectric polarization can be obtained as 1.86×10^{-14} J. Therefore the corresponding energy conversion efficiency ($\eta = W_E/W_M$) is found to be ~5.08% for $\varepsilon = 0.53\%$ ($W_M = 3.66 \times 10^{-13}$ J).

Strain-modulated carrier transport in the MoS_2 piezotronic effect and piezoresistive effect. The observed difference in conduction behaviour under strain between monolayer and bilayer/bulk MoS_2 is attributed to their fundamental distinction in crystal symmetries. It has been theoretically predicted that MoS_2 with odd number of layers (point group D_{3h}) will exhibit intrinsic piezoelectric property as a result of its lack of centrosymmetry in crystal structure, whereas piezoelectricity will vanish in centrosymmetrically structured MoS_2 with an even number of layers (point group D_{6h})[9,10,16]. Resulting from changes in band structure, charge carrier density or the density of states in the conduction band of strained semiconductor materials, the piezoresistive effect is symmetrical on the two end contacts and has no polarity; this will not produce the function of a transistor. Piezoresistance is a common feature of semiconductors such as Si and GaAs and is not limited to piezoelectric semiconductors. The strain-induced modification of band structures in MoS_2 has recently been reported with a small range of compressive strain (<2%) increasing and tensile strain decreasing the bandgap for MoS_2, as a result of the change in orbital overlap and hybridization by strain[33–36]. The trigonal-prismatic coordination between the molybdenum and sulphur atoms and the absence of inversion symmetry give rise to piezoelectric polarization in strained monolayer MoS_2, with the polarization charges induced at the zigzag edges. In general, the negative piezoelectric polarization charges, and hence the negative piezopotential induced at the semiconductor side near the interface of the local contact formed between the metal electrode and an n-type semiconductor, can repel the electrons from the interface, resulting in a further depleted interface and increased local barrier heights, whereas the positive piezoelectric polarization charges and hence the positive piezopotential created at the semiconductor side near the interface can attract the electrons towards the interface, resulting in a less depleted interface and hence decreased local barrier heights. The strain-induced polarization charges can therefore directly affect the local contacts at the metal–MoS_2 interfaces by exerting substantial influences on the concentration and distribution of free carriers in MoS_2 as well as on the modulation of electronic charge in interface states or metal. The observed anisotropic changes in current transport with applied strain are associated with variations in Schottky barrier height (SBH) tuned by both the strain-induced change in band structure and piezoelectric polarization charges at a reverse-biased Pd–MoS_2 barrier[37]. The contributions to changes in SBH at source and drain contacts from the band structure effect share the same polarity: uniaxial compressive (<2%) or tensile strain in the direction along armchair edge increases or decreases the bandgap for monolayer MoS_2 (refs 33–36), whereas the modulation of SBHs at both contacts due to the polarization-induced surface charges and the corresponding adjustment of electronic states at the interface possess the opposite polarities owing to the polarity of induced piezoelectric charges[37]. These piezoelectric polarization charges can effectively modulate the local contact characteristics through an internal field, depending on doping type, carrier density and the crystallographic orientation of the piezoelectric semiconductor material as well as on the polarity of the applied strain. Consequently, the transport of charge carriers across the metal–semiconductor contact can be effectively modulated by the piezoelectric polarization charges, which can be controlled by varying the magnitude and polarity of the externally applied strain. The modulation or gating of the charge transport across the interface by the strain-induced polarization charges is the core of piezotronics. The gauge factor

$([\Delta I(\varepsilon)/I(0)]/\Delta\varepsilon)$ of the monolayer MoS_2 device for strain sensing has also been characterized; the highest value is ~760, which exceeds the values of conventional metal strain gauges (~1–5), a state-of-the-art silicon strain sensor (~200) and a graphene strain sensor (~300)[26], suggesting the potential for using monolayer MoS_2 in highly sensitive strain sensing. The higher gauge factor in a monolayer MoS_2 strain sensor than those for graphene, bilayer MoS_2 (~230) and bulk MoS_2 (~200) is attributed to enhancement by piezoelectric polarization. However, we are not sure why bilayer devices show slightly higher gauge factors than bulk samples. We think that relative change in carrier density and/or mobility by strain is more significant in bilayer devices than in bulk samples, which may be related to the difference between the band structures of bilayer and bulk MoS_2. Last, the effect from substrate contact with the bilayer structure may also contribute to the observed large piezoresistance of the device. Moreover, the much smaller thickness and original conductivity in bilayer devices may also have a role here. Both theoretical calculations (for example, tight binding) and experimental characterizations are required for a better understanding of the piezoresistive effect in bilayer MoS_2.

Internal screening of piezoelectric polarization charges in MoS_2 by free carriers. The partial screening of strain-induced polarization charges by free carriers has been widely observed for conventional piezoelectric semiconductors such as ZnO (refs 38, 39). Because MoS_2 has a relatively small bandgap (~ 1.8 eV), it is anticipated that the internal screening of piezoelectric charges should exist. Considering the *n*-type doping characteristics of MoS_2, the positive polarization charges induced by strain will be partly screened by the free electrons in MoS_2, whereas the negative polarization charges will be preserved. Therefore it is still possible to observe piezoelectric power output and piezotronic transport. The trend in band diagrams shown in Fig. 3c is still valid if the MoS_2 is not heavily doped, except that the changes in SBH induced by positive piezoelectric charges will be decreased. Considering the much smaller dimensions of 2D materials than those of conventional piezoelectric semiconductors such as ZnO nanowires, the carrier density or even conductivity type in monolayer MoS_2 may be affected or modulated in a more efficient or sensitive way by substitutional doping at both the Mo and the S sites and by the adsorption of charged molecules. More in-depth investigations are therefore needed in both theory and experiments to quantify the effect of internal screening of piezoelectric polarization in 2D piezoelectric semiconductors.

31. Landau, L. D., Lifshits, E. M., Kosevich, A., d. M. & Pitaevskiĭ, L. P. *Theory of Elasticity* 3rd English edn (Pergamon, 1986).
32. Cooper, R. C. *et al.* Nonlinear elastic behavior of two-dimensional molybdenum disulfide. *Phys. Rev. B* **87,** 035423 (2013).
33. He, K., Poole, C., Mak, K. F. & Shan, J. Experimental demonstration of continuous electronic structure tuning via strain in atomically thin MoS_2. *Nano Lett.* **13,** 2931–2936 (2013).
34. Conley, H. *et al.* Bandgap engineering of strained monolayer and bilayer MoS_2. *Nano Lett.* **13,** 3626–3630 (2013).
35. Hui, Y. Y. *et al.* Exceptional tunability of band energy in a compressively strained trilayer MoS_2 sheet. *ACS Nano* **7,** 7126–7131 (2013).
36. Johari, P. & Shenoy, V. B. Tuning the electronic properties of semiconducting transition metal dichalcogenides by applying mechanical strains. *ACS Nano* **6,** 5449–5456 (2012).
37. Zhang, Y., Liu, Y. & Wang, Z. L. Fundamental theory of piezotronics. *Adv. Mater.* **23,** 3004–3013 (2011).
38. Gao, Y. F. & Wang, Z. L. Equilibrium potential of free charge carriers in a bent piezoelectric semiconductive nanowire. *Nano Lett.* **9,** 1103–1110 (2009).
39. Hu, Y. F., Lin, L., Zhang, Y. & Wang, Z. L. Replacing a battery by a nanogenerator with 20 V output. *Adv. Mater.* **24,** 110–114 (2012).

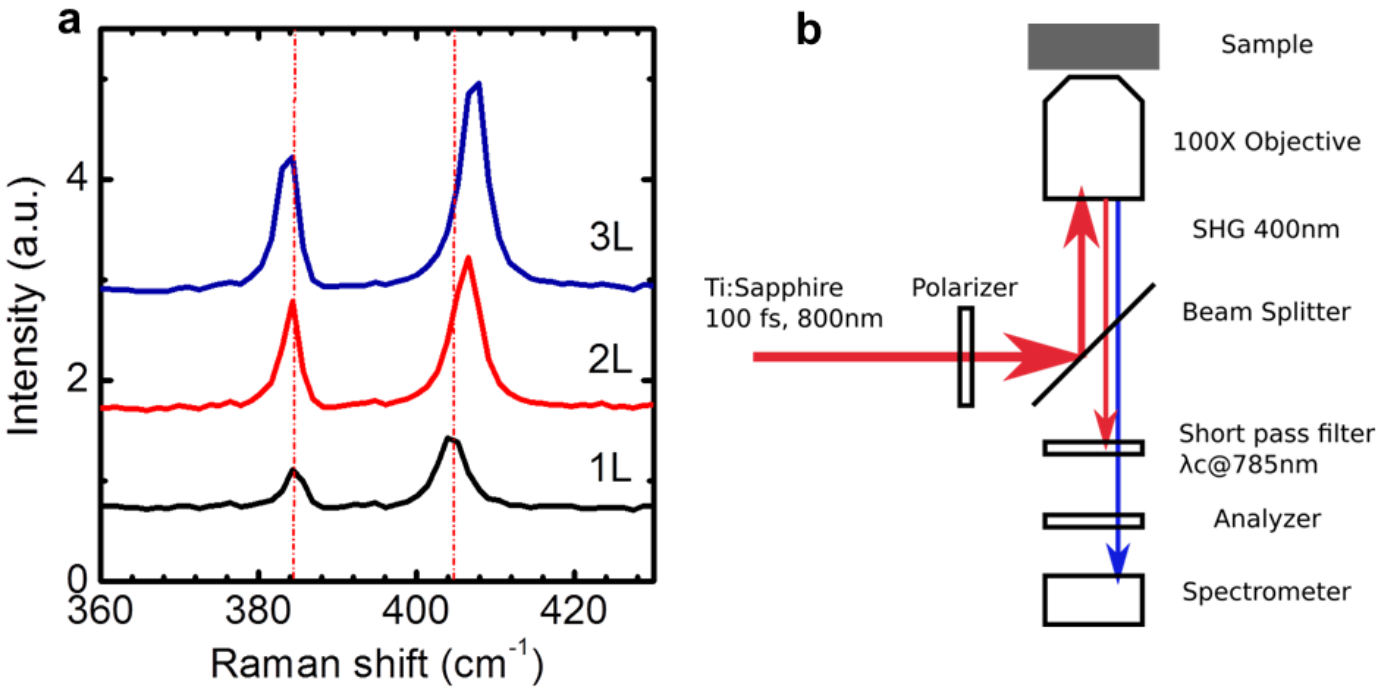

Extended Data Figure 1 | Raman spectrum of MoS_2 flakes and setup for SHG measurement. **a**, Raman spectrum of MoS_2 flakes with different layer numbers. **b**, Experimental setup for the SHG measurement.

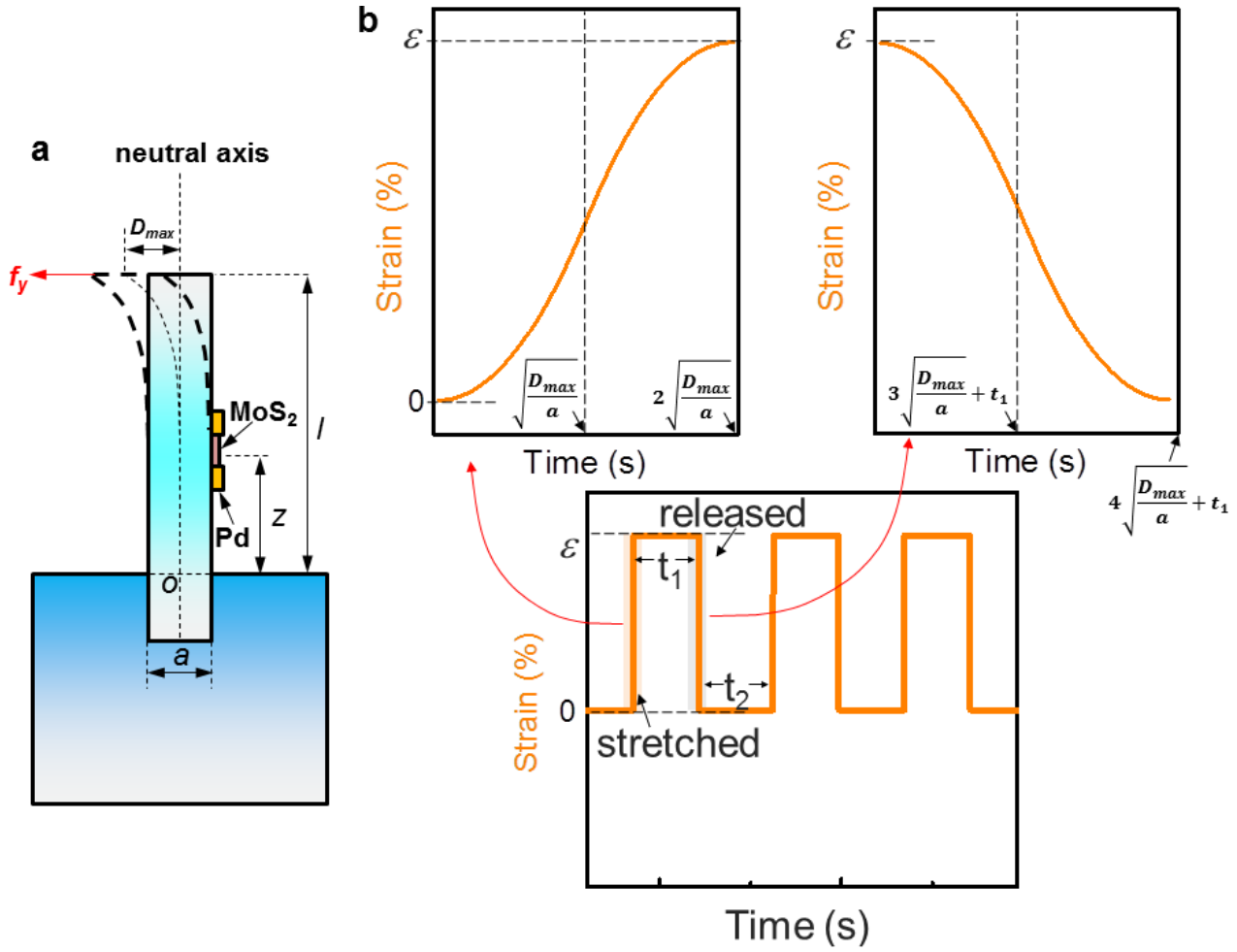

c Stretching

Name	Value
Position	10 mm
Acceleration	5 m/s^2
Deceleration	5 m/s^2

Releasing

Name	Value
Position	0 mm
Acceleration	5 m/s^2
Deceleration	5 m/s^2

Holding

Name	Value
Rise Position Wait Time	1000 ms
Fall Position Wait Time	1000 ms

Extended Data Figure 2 | Mechanical strain applied to MoS_2 device. **a**, Schematic drawing for estimating strain in MoS_2 device. **b**, Schematic plot of strain driving signal from linear motor. **c**, Typical configurations for linear motor.

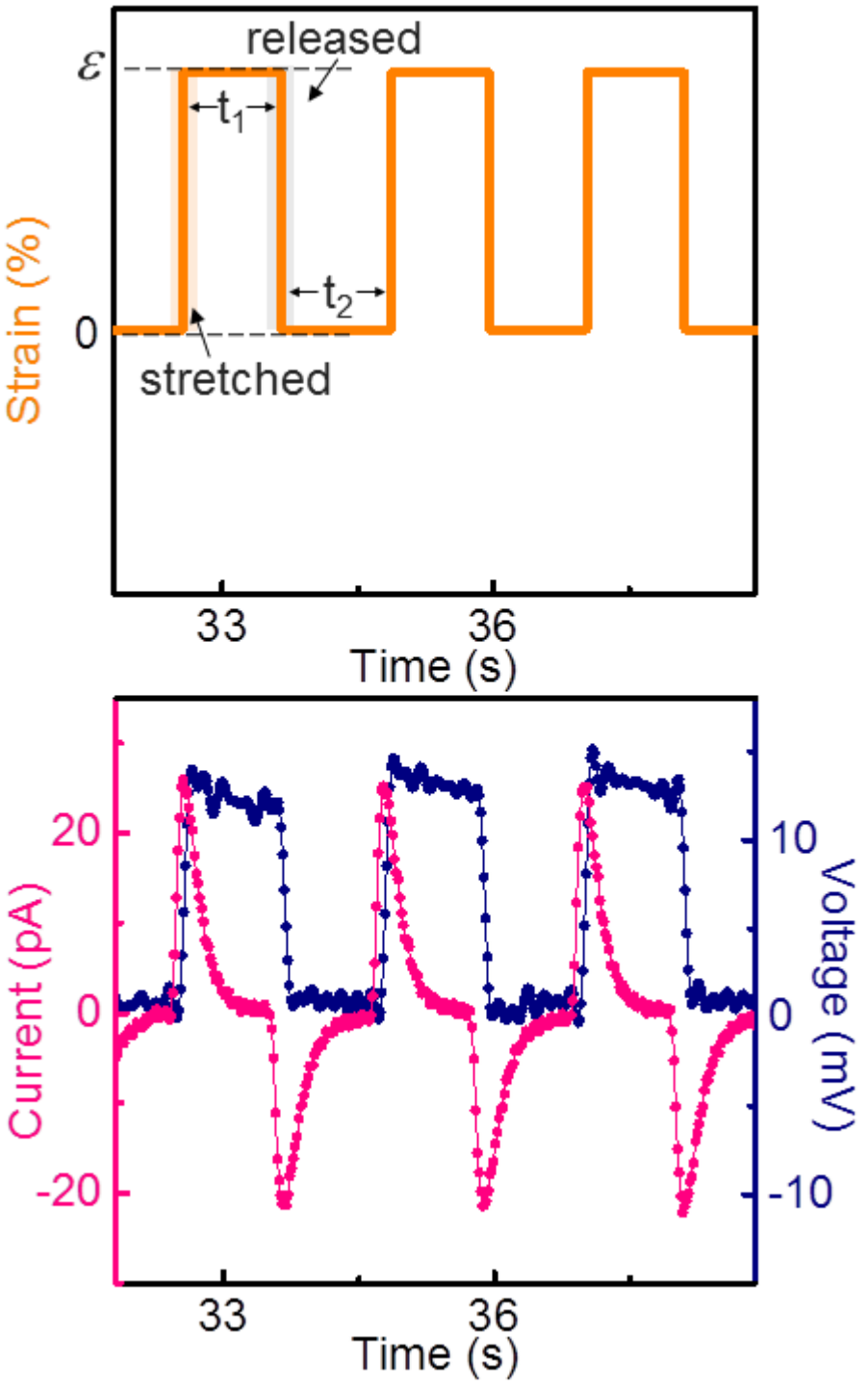

Extended Data Figure 3 | Piezoelectric open-circuit voltage and short-circuit current.

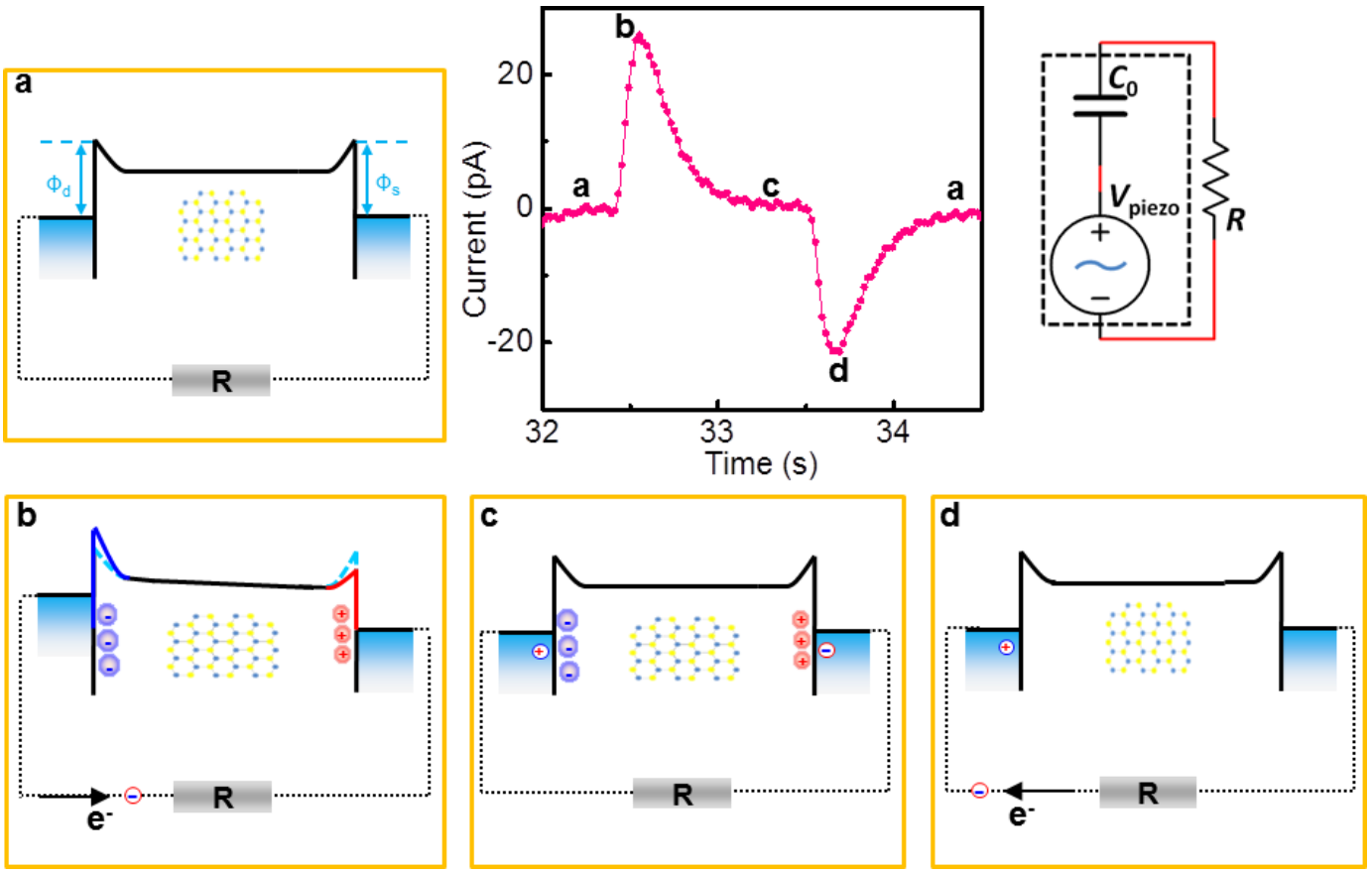

Extended Data Figure 4 | Mechanism of electrical power generation in single-layer MoS_2 due to the flow of electrons in external load driven by piezoelectric polarization charges. The equivalent circuit of the piezoelectric nanogenerator is also shown.

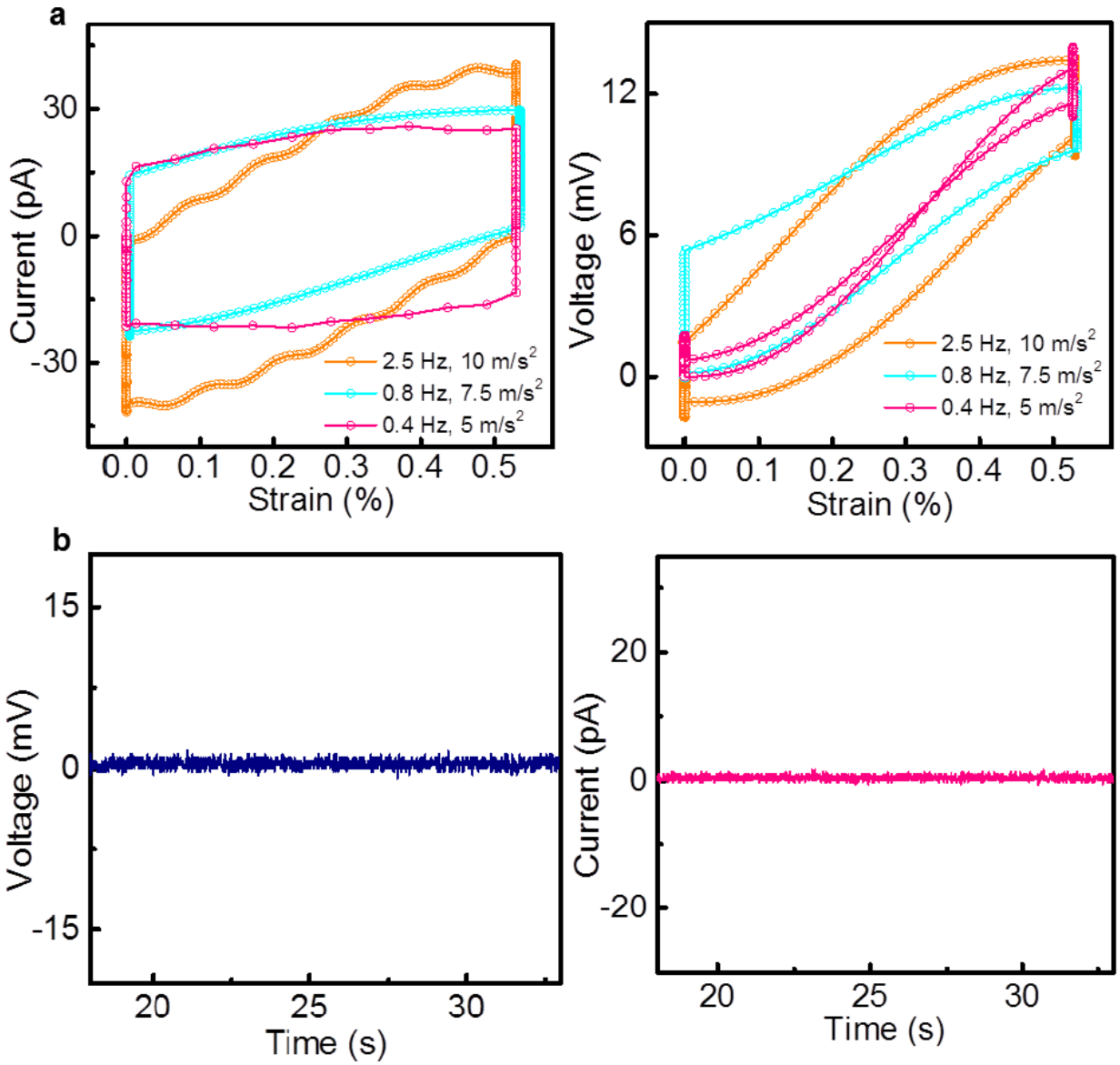

Extended Data Figure 5 | Piezoelectric output of MoS_2 device with different strain parameters. **a**, Short-circuit current–strain and open-circuit voltage–strain hysteresis loops. Hold time $t_1 = t_2 = 1$ s and acceleration $a = 5\ \mathrm{m\,s^{-2}}$ for the curve of 0.4 Hz; hold time $t_1 = t_2 = 0.5$ s and acceleration $a = 7.5\ \mathrm{m\,s^{-2}}$ for 0.8 Hz; hold time $t_1 = t_2 = 0.1$ s and acceleration $a = 10\ \mathrm{m\,s^{-2}}$ for 2.5 Hz. **b**, Electrical outputs from bare PET substrate without single-layer MoS_2 under periodic strain (0.53%).

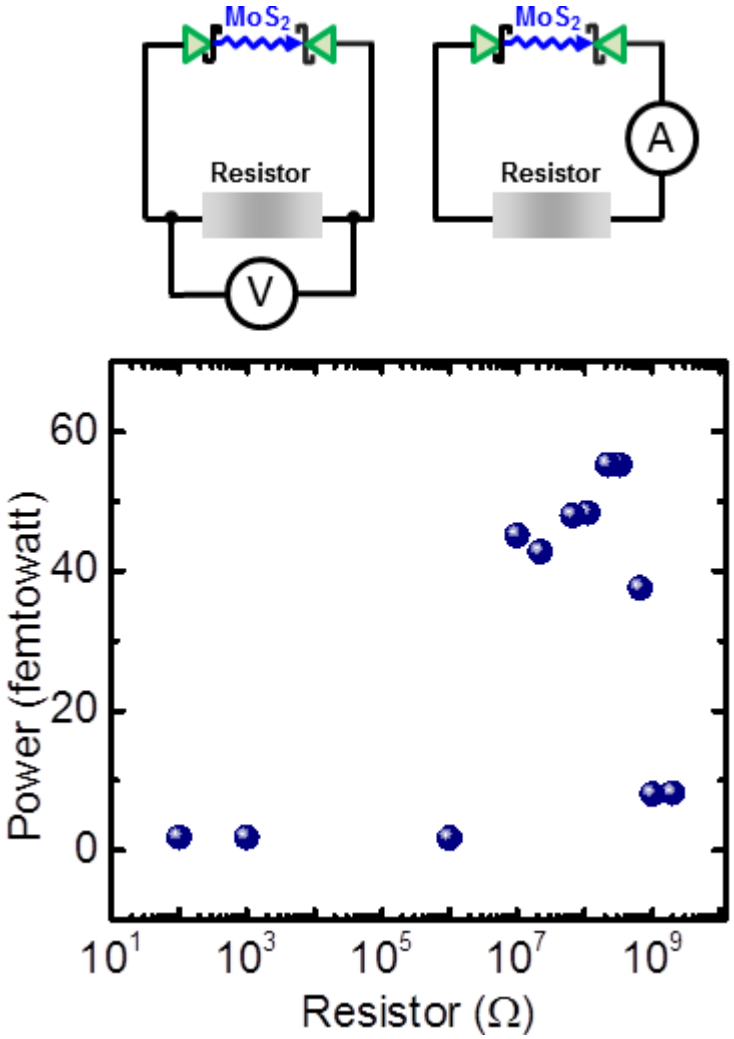

Extended Data Figure 6 | Circuit connection for measuring the power outputs on the external load and power delivered to the load at 0.53% strain.

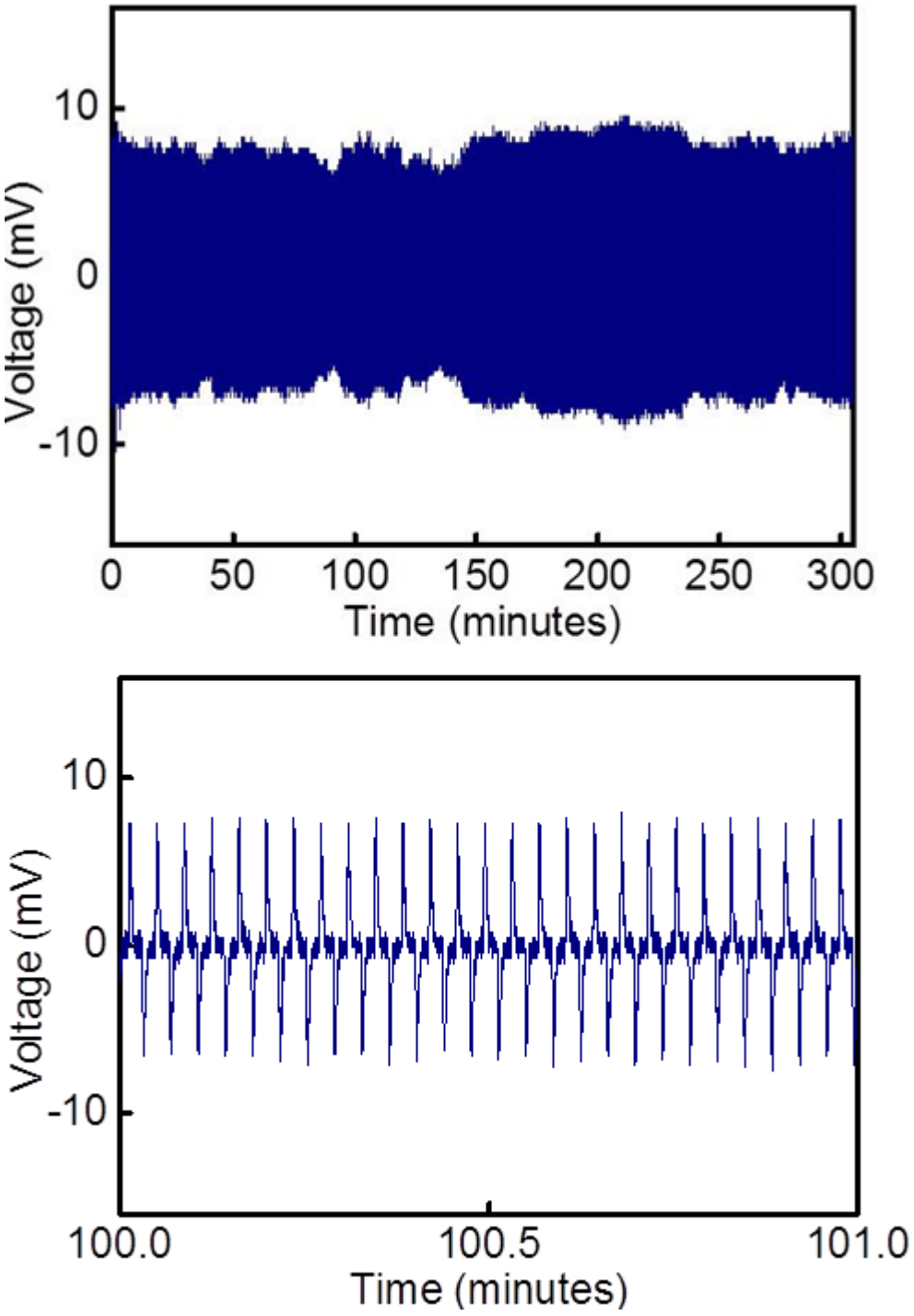

Extended Data Figure 7 | Stability test of voltage output from single-layer MoS_2 device. The frequency of 0.5 Hz was held for 300 min. The results demonstrate good stability of the device in mechanical energy harvesting for prolonged periods.

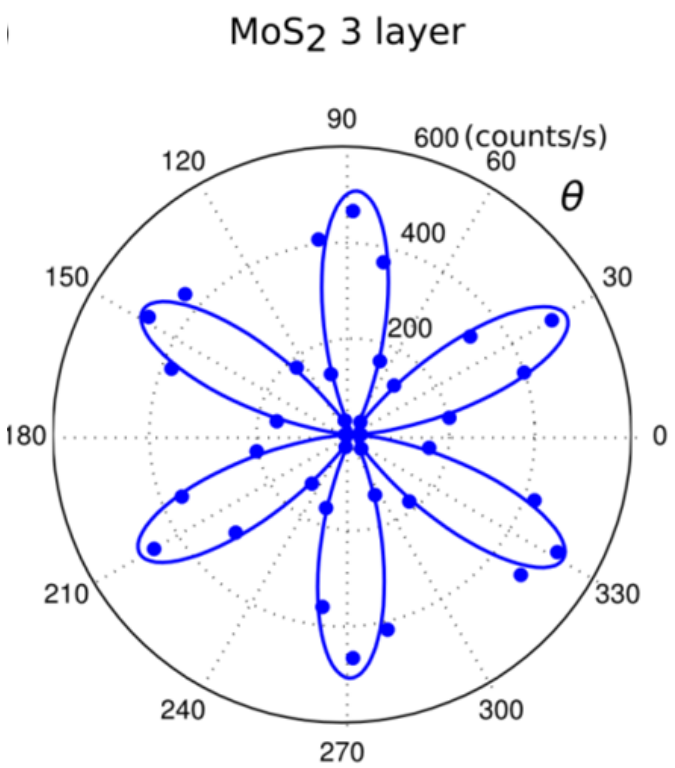

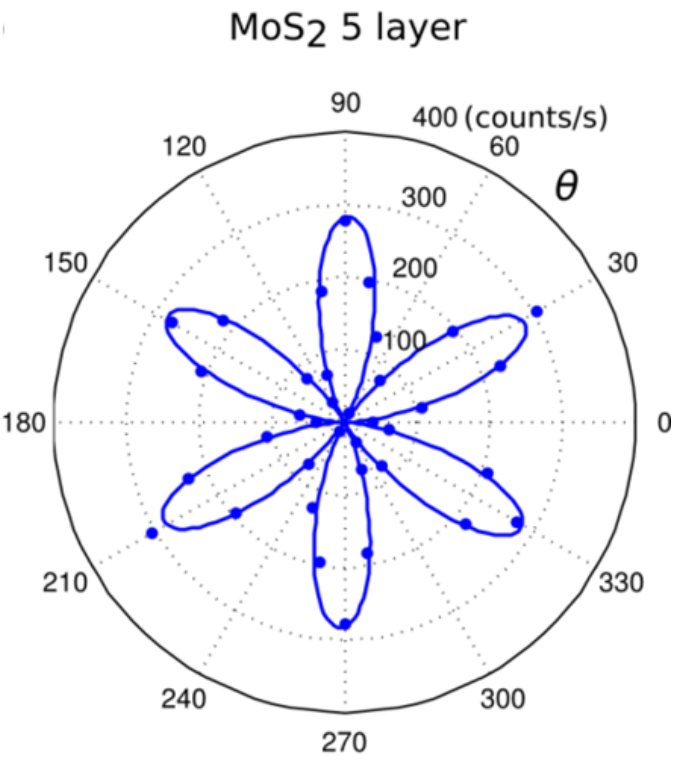

Extended Data Figure 8 | Angular dependence of SHG intensity (perpendicular component) for three-layer and five-layer MoS_2. Samples of even layers (two, four and six layers) give vanishing SHG intensity regardless of their crystallographic orientation. θ denotes the angle between the fundamental light polarization and the mirror plane of the lattice.

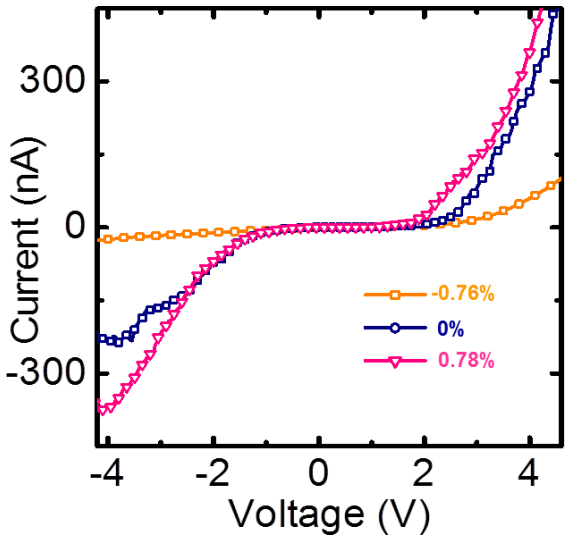

Extended Data Figure 9 | Transport characteristics of bulk device under different uniaxial strains.

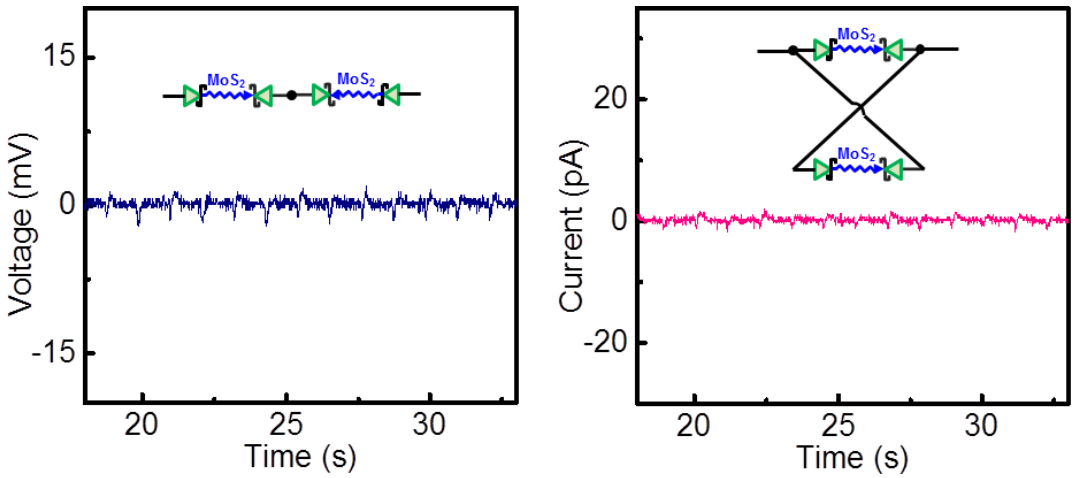

Extended Data Figure 10 | Electrical outputs when CVD devices 1 and 2 are destructively connected.